UC Irvine
UC Irvine Previously Published Works

Title

Lookup-table method for imaging optical properties with structured illumination beyond the diffusion theory regime

Permalink

https://escholarship.org/uc/item/9xx66195

Journal

Journal of Biomedical Optics, 15(3)

ISSN

1083-3668

Authors

Erickson, Tim A
Mazhar, Amaan
Cuccia, David
et al.

Publication Date

2010

DOI

10.1117/1.3431728

Copyright Information

Peer reviewed

Lookup-table method for imaging optical properties with structured illumination beyond the diffusion theory regime

Tim A. Erickson
University of Texas
Department of Biomedical Engineering
107 W Dean Keeton
Austin, Texas 78712

Amaan Mazhar
Beckman Laser Institute
1002 Health Sciences Road
Irvine, California 92617-3010

David Cuccia
Modulated Imaging, Inc.
1002 Health Sciences Road
Irvine, California 92617-3010

Anthony J. Durkin
Beckman Laser Institute
1002 Health Sciences Road
Irvine, California 92617-3010

James W. Tunnell
University of Texas
Department of Biomedical Engineering
107 W Dean Keeton
Austin, Texas 78712

Abstract. Sinusoidally structured illumination is used in concert with a phantom-based lookup-table (LUT) to map wide-field optical properties in turbid media with reduced albedos as low as 0.44. A key advantage of the lookup-table approach is the ability to measure the absorption (μ_a) and reduced scattering coefficients (μ_s') over a much broader range of values than permitted by current diffusion theory methods. Through calibration with a single reflectance standard, the LUT can extract μ_s' from 0.8 to 2.4 mm^{-1} with an average root-mean-square (rms) error of 7% and extract μ_a from 0 to 1.0 mm^{-1} with an average rms error of 6%. The LUT is based solely on measurements of two parameters, reflectance R and modulation M at an illumination period of 10 mm. A single set of three phase-shifted images is sufficient to measure both M and R, which are then used to generate maps of absorption and scattering by referencing the LUT. We establish empirically that each pair (M, R) maps uniquely to only one pair of (μ_s', μ_a) and report that the phase function (i.e., size) of the scatterers can influence the accuracy of optical property extraction. © *2010 Society of Photo-Optical Instrumentation Engineers.* [DOI: 10.1117/1.3431728]

1 Introduction

The concept of employing periodic structured illumination to characterize the optical properties of high-albedo ($\mu_s'/\mu_a > 10$), turbid samples is well established. Cuccia et al. have previously demonstrated a wide-field imaging technique referred to as spatial frequency domain imaging (SFDI) or modulated imaging.[1] This imaging approach isolates the sample's frequency-dependent modulated reflectance at each image pixel (x, y), which facilitates sample analysis in the spatial frequency domain[1,2] and corresponding optical property extraction. In order to generate maps of the absorption (μ_a) and reduced scattering (μ_s') coefficients, the frequency-dependent modulated reflectance is either fit to the standard diffusion approximation (SDA) or analyzed using a two-frequency Monte Carlo–based lookup table (LUT).[3]

SFDI is being developed for a variety of clinically relevant applications, including optical property mapping to assist in laser tattoo removal[4] and characterization of layered tissue.[5] Gioux et al. have successfully combined phase profilometry measurements in parallel with SFDI, in order to correct for the effect of surface geometry on the measured diffuse reflectance.[6] This technique facilitates accurate optical property extraction of objects with complex geometries, highlighting the potential of using SFDI for quantitative clinical imaging. The capability of SFDI to simultaneously measure surface geometry and extract localized optical properties over wide fields of view may prove to be particularly useful for a variety of applications, including machine vision-assisted surgery[7] and the detection of epithelial dysplasia.[8]

SFDI employing the SDA provides exceptional accuracy in extracting the optical properties of samples where the reduced scattering coefficient exceeds the absorption coefficient by a factor of eight or more. However, the accuracy of SDA is rapidly compromised when $(\mu_s'/\mu_a) < 8$. This is the optical property regime, where diffusion theory predictions begin to diverge rapidly from experimental results.[9] It has been established that (μ_s'/μ_a) in human tissue at visible wavelengths is often much less than 8, particularly at wavelengths of 540 and 576 nm, corresponding to the absorption peaks of hemoglobin, where (μ_s'/μ_a) approaches unity.[10,11] To our knowledge, there have been no published studies evaluating the potential of using a SFDI system to characterize low-albedo turbid me-

Address all correspondence to: Tim A. Erickson, University of Texas, Department of Biomedical Engineering, 107 West Dean Keeton, Austin, Texas 78712. Tel: 720-341-8280; Fax: 512-471-0616; E-mail: tim.erickson@mail.utexas.edu

dia with $(\mu_s'/\mu_a) < 3$. Here, we demonstrate an empirical, phantom-based LUT, which extends the range of optical properties that can be measured with a SFDI system beyond the diffusion theory regime. The phantom-based LUT can extract the optical properties of turbid media with (μ_s'/μ_a) as low as unity. Although a Monte Carlo–based LUT should offer comparable performance, the phantom-based LUT is advantageous in that it is based on experimental measurements and is automatically calibrated to the illumination and collection geometry of a real optical system. The LUT is based on measurements of reflectance R and modulation M, which are related to but distinct from the measured parameter (modulated reflectance) used in the SFDI 2-frequency Monte Carlo LUT.[2]

The present approach is strongly motivated by the work of Rajaram et al. and Reif et al., who have demonstrated distinct empirical approaches for accurately measuring optical properties beyond the diffusion regime with fiber-optic probes.[12,13] Although such probe-based systems are ideal for interrogating small volumes of tissue and particularly useful for performing intracorporeal measurements, they have two drawbacks. First, they are not readily capable of mapping optical properties over wide fields of view. For example, a probe with a 300 μm source detector separation would have to be scanned by more than 96,000 points in order to render a 12×8 cm map of the optical properties, whereas only three CCD-based images are required for the phantom-based LUT. Second, optical probes are typically placed in contact with tissue, which can confound the measurement process. Pressure-induced changes in tissue due to contact at the probe-tissue interface can result in large errors in the extracted optical properties. Reif et al. have reported errors of $>80\%$ in the reduced scattering coefficient for probe pressures as low as 0.2 N/mm^2.[14]

The SFDI system is inherently capable of both wide-field and noncontact optical property measurements. In this work, we demonstrate how a phantom-based LUT can be used to extend the range of optical properties that can be readily measured using a SFDI system, while employing a single calibration standard. The effect of scatterer phase function on extracting (μ_s'/μ_a) with the LUT is reported.

2 Experimental Design

2.1 Instrumentation and Acquisition

We constructed a custom SFDI system similar to the one first described in detail by Cuccia et al.[1] A diagram of the system is shown in Fig. 1. The system consists of a high-intensity 150 W Xenon Newport lamp (model no. 67005) stabilized by a Newport power supply (model no. 69907). Light emanating from the lamp is projected through a series of lenses (L1,L2) onto a digital micromirror device [(DMD) Discovery 1100, Texas Instruments, Dallas, Texas].

The DMD, a spatial light modulator, consists of 1024 $\times$768 micromirrors, which rapidly rotate into "on" and "off" positions, in order to produce gray-scale patterns with 8-bit resolution. The mirrors are controlled with a ViALUX ALP chipset (Sachsen, Germany), which is configured in Labview (National Intruments, Austin, Texas).

The light reflected from the DMD is imaged onto the sample of interest by converging lens L3. The sample is placed on a movable stage to facilitate proper focusing. On its
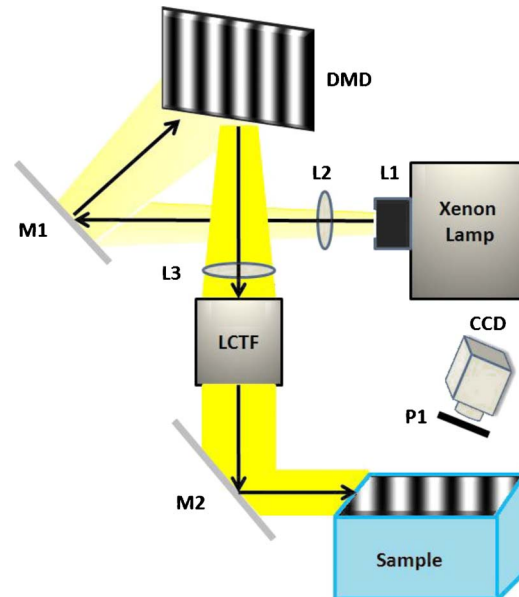

Fig. 1 Experimental setup: Light from the Xe lamp is reflected from the DMD and imaged onto the sample after passing through a liquid-crystal tunable filter (LCTF). The diffuse reflectance is captured by the CCD, which is positioned at a slight angle, in order to avoid the collection of specularly reflected photons.

path toward the sample, the light passes through a narrow-band, polarizable liquid-crystal tunable filter (Meadowlark Optics, Frederick, Colorado, Part No TOF-VIS) and is reflected from a 45-deg mirror (M2). The projected field is approximately 12×8 cm. An inexpensive, noncooled Firewire CCD camera (AVT Stingray 145B, Graftek Imaging, Austin, Texas) is positioned immediately to the right of the mirror, in order to image the diffusely reflected photons.

In order to avoid imaging specular reflections, the camera's optical axis is held at a slight angle (<5 deg) relative to the sample normal. For rough surfaces, a linear polarizer (P1) must be placed directly in front of the camera lens and rotated 90 deg relative to polarization axis of the LCTF to avoid imaging specularly reflected photons. In the interest of reducing acquisition time, a polarizer was not used in our experiments because the camera angle employed was sufficient to avoid collection of specularly reflected photons from flat, liquid samples. As a cross-check, several experiments were carried out with P1 in place and compared to results to P1 removed. Differences in modulation and reflectance were found to be $<1\%$ at a spatial period of 10 mm.

In order to produce a high-intensity, uniform illumination over the entire optical field, the adaptive optics capabilities of the DMD were exploited. To correct for intensity deviations of up to 20% in the initial illuminated field, the base projection $B(x,y)$ of the DMD was reconfigured. Patterns on the DMD are formed by assigning an 8-bit value (0–255) to each micromirror. The initial base projection $B_i(x,y)$ was set so that each micromirror had a value of 200 $[B_i(x,y)=200]$. An image $I_i(x,y)$ of a large silvered mirror was recorded with base projection $B_i(x,y)$, where micromirror (x,y) corresponds to image pixel (x,y). With $I_i(x,y)$ normalized to have a maximum value of 1, the reconfigured base projection was calcu-

lated as $B(x,y)=B_i(x,y)/I_i(x,y)$. This approach yielded a highly uniform projected field with maximum reflectance deviations of $<1\%$, and a full-field standard deviation of 0.36%.

Image acquisition was fully automated in LabVIEW. For a given sample, the modulation $M(x,y,f_x)$ and dc reflectance $R(x,y)$ were acquired as follows. A two-dimensional sinusoidally modulated intensity pattern of the form

$$P(x,y,f_x) = 0.5B(x,y)[\sin(2\pi f_x x + \phi) + 1]$$

is rendered on the DMD and projected onto the sample. As in SFDI, three images (I_1,I_2,I_3) of the sample are acquired at phase projections of $\phi=0, 2\pi/3, 4\pi/3$, respectively. A back-ground image I_{BK} is subtracted from each of the three images to correct for effects of dark current and stray light from the lamp. Room lighting was turned off during image acquisition to maximize the signal to noise ratio. In order to take advantage of the full dynamic range of the CCD, exposure times were adjusted from 0.1 to 1 s, depending on sample albedo, resulting in sequence acquisition times of $1-3$ s. All images were normalized for exposure time.

2.2 Definitions of Modulated Reflectance, Modulation, and Reflectance

The magnitudes of the ac $[I_{ac}(x,y,f_x)]$ and dc $[I_{DC}(x,y)]$ components of the diffuse reflectance are given by

$$I_{ac}(x,y,f_x) = \frac{\sqrt{2}}{3}\sqrt{[I_1(x,y,f_x) - I_2(x,y,f_x)]^2 + [I_2(x,y,f_x) - I_3(x,y,f_x)]^2 + [I_3(x,y,f_x) - I_1(x,y,f_x)]^2}$$

$$I_{dc}(x,y) = [I_1(x,y) + I_2(x,y) + I_3(x,y)]/3.$$

In the SFDI approach defined by Cuccia et al.,[1] the key parameter measured is the modulated reflectance, R_d, at the sample region corresponding to camera pixel (x,y) and frequency f_x defined as

$$R_d(x,y,f_x) = \frac{I_{ac,measured}(x,y,f_x)}{I_{ac,reference}(x,y,f_x)}R_{d,predicted}(x,y,f_x),$$

where $I_{ac,measured}$ is the measured ac magnitude of the sample; $I_{ac,reference}$ is the measured ac magnitude of a reference phantom with known optical properties, and $R_{d,predicted}$ is the predicted diffuse reflectance of the reference phantom. The optical properties, μ_s' and μ_a, are extracted by fitting R_d to a forward model based on diffusion theory or by fitting R_d to data from Monte Carlo simulations.[2]

In the phantom-based LUT approach, the measured parameters are the frequency-dependent modulation $M(x,y,f_x)$ and the absolute diffuse reflectance $R(x,y)$. A 99% reflectance Spectralon (Labsphere, North Sutton, New Jersey) is employed as the calibration standard, in order to simultaneously measure R and correct for the effect of the modulation transfer function of the imaging system on the measured modulation M. The present approach is distinct from previous work[1] in that optical property extraction is based purely on empirical measurements rather than simulations or model-based fitting.

We define the two key parameters of the LUT in terms of the measured ac and dc intensity values of the sample $(I_{dc,sample}; I_{ac,sample})$ and 99% Spectralon $(I_{dc,spectralon}; I_{ac,spectralon})$ as follows:

$$R(x,y) = \frac{I_{dc,sample}(x,y) \times 0.99}{I_{dc,spectralon}(x,y)}$$

$$M(x,y,f_x) = \frac{I_{ac,sample}(x,y,f_x)/I_{dc,sample}(x,y,f_x)}{I_{ac,spectralon}(x,y,f_x)/I_{dc,spectralon}(x,y,f_x)}.$$

2.3 LUT Phantoms

We created a LUT based on measurements of M and R in liquid phantoms for each of the following spatial frequencies $f_x=0.5, 0.25, 0.167, 0.125, 0.1, 0.0833$, and 0.0713 mm^{-1}, which correspond to spatial periods of 2, 4, 6, 8, 10, 12, and 14 mm, respectively. For all measurements, the filter wavelength was set to 540 nm (FWHM=5 nm). Because the LUT is wavelength independent, any wavelength at sufficient signal to noise levels could have been selected.

Each 30- mL phantom was prepared as homogeneous solution of deionized water, India ink (Sallis International, Golden, Colorado) as the absorber, and 0.35-μm-diam polystyrene microspheres ($n=1.59$) as the scatterer (Polysciences, Warrington, Pennsylvania). As described in Section 3.3, 0.35- μm spheres were selected because they were found to minimize overall LUT error, and 0.35 μm microspheres have an anisotropy value of $g=0.75$, which is slightly below the value of $g=0.82$ for human dermis reported by Prahl et al.[15]

For all phantoms, the absorption and reduced scattering coefficients were assumed to vary linearly with ink and microsphere concentration, consistent with the results of Cubeddu et al.[16] The reduced scattering coefficient of the spheres was calculated using the Mie theory code of Bohren and Hoffman,[17] and the absorption coefficient of the ink was measured using a Beckman Coulter spectrophotometer (Fullerton, California). For clarity, the absorption and reduced scattering coefficients in units of millimeters are calculated as

$$\mu_s' = (1 - g)\rho\sigma_s,$$

$$\mu_a = \frac{-\ln(T)}{10},$$

where g is the solid-angle average cosine of the scattering phase function; ρ is the number density of scatterers in units of (particles per cubic millimeter); σ_s is the scattering cross section, and T is the transmittance of a sample placed in a cuvette with a 1-cm path length.

One-hundred twenty-six phantoms were formulated in order to satisfy all of the following combinations of absorption and scattering coefficients: μ_a=0, 0.01 0.033, 0.066, 0.10, 0.20, 0.30, 0.40, 0.50, 0.60, 0.70, 0.80, 0.90, and 1.0 mm^{-1} and μ_s'=0.80, 1.00, 1.20, 1.40, 1.60, 1.80, 2.00, 2.20, and 2.40 mm^{-1}. This range of optical property values was selected to cover a large range of values characteristic of human tissue at visible wavelengths.[10,11] To ensure homogeneity, phantoms were vortexed for roughly 30 s in a closed vial, poured into a large Petri dish, and then briefly mixed with a clean pipette tip prior to measurement. Phantom depth was ~1.5 cm. The measured modulated reflectance was identical when a larger 3.0-cm phantom with μ_s'=1.0 and μ_a=0 mm^{-1} was employed; thus, sample depth was assumed to be sufficient to mimic a semi-infinite medium. The measurement stage was painted matte black, in order to avoid stray back reflections.

With the intent of maximizing LUT accuracy, three frames at each illumination phase were averaged and then used to calculate M and R at each pixel (x, y). To further increase the signal-to-noise ratio and remove edge effects (due to the finite extent of the illumination), we averaged values from a 200 $\times$ 200 pixel region in the center of the image. These averaged values were used to establish M and R for the LUT.

2.4 Validation Studies

In order to evaluate the accuracy of the LUT, we performed measurements on three sets of liquid-validation phantoms. In the first set, the absorber was switched from India ink to Red 40 food coloring (McCormick, Hunt Valley, Maryland), while the scatterer remained the same (0.35-μm spheres). The absorption coefficient, μ_a, was varied from 0 to 1 mm^{-1}, while the reduced scattering coefficient, μ_s', was held constant at 1.5 mm^{-1}. In the second validation set, μ_s' was varied from 0.8 to 2.4 mm^{-1} with μ_a held constant at 0.5 mm^{-1}. Once again, Red 40 was used as the absorber and 0.35 μm spheres as the scatterer. In the third validation set, we investigated the effect of sphere size (phase function) on the recovered optical properties. In this set of experiments, μ_s' was held constant at 1.0 mm^{-1} and μ_a was varied from 0 to 0.8 mm^{-1}. Measurements were performed on phantoms formulated using polystyrene spheres with diameters of 0.456, 1.02, 1.53, and 2.07 μm. Table 1 summarizes the validation experiments performed.

The validation experiments were carried out as follows. Whereas, a 200$\times$200 pixel region was binned to construct the LUT, for validation, a much smaller 5$\times$5 region located in the center of the illumination was binned, in order to pro-

Table 1 Physical parameters used for the tissue phantoms validation sets.

Set No.	Absorber	Scatterer	μ_s' (mm^{-1})	μ_a (mm^{-1})
1	Red 40	0.35 μm spheres	1.5	0–1.0
2	Red 40	0.35 μm spheres	0.8–2.4	0.5
3	India Ink	Multiple sizes	1.0	0–0.8

vide both spatial resolution and an acceptable signal-to-noise ratio. As before, three images at each phase shift were averaged.

For direct comparison to SDA, the same set of images was used to extract phantom optical properties from measurements of the modulated reflectance for each f_x by fitting the measured modulated reflectance to the diffusion theory model first introduced by Cuccia et al.[2] For the calibration reference phantom, a liquid phantom (0.35-μm spheres+India ink) with optical properties of (μ_s'=1.00 mm^{-1} and μ_a=0.033 mm^{-1}) was used. In order to provide a relevant comparison to SDA optical property extraction, an eight-frequency LUT was evaluated in addition to the two-frequency LUTs [one for each nonzero f_x+dc (f_x=0)]. This was done to investigate the effect of spatial frequency on LUT accuracy.

The LUTs were implemented by first interpolating both $M(\mu_s', \mu_a)$ and $R(\mu_s', \mu_a)$ using linear interpolation, in order to provide optical property resolution of 0.005 mm^{-1} in both μ_s' and μ_a. For optical property extraction, a constrained nonlinear optimization routine (Matlab function "fmincon") was used to find the optimal pair (μ_s', μ_a), which minimizes the difference between the measured modulation and reflectance and the modulation and reflectance corresponding to (μ_s', μ_a) at each frequency f_x. Mathematically, this is defined as

$$\min\left\{ \sum_{f_x} \left[\sqrt{\left(\frac{M_{measured}(f_x) - M_{(LUT:u_s', u_a)}(f_x)}{M_{(LUT:u_s', u_a)}(f_x)} \right)^2} + \sqrt{\left(\frac{R_{measured}(f_x) - R_{(LUT:u_s', u_a)}(f_x)}{R_{(LUT:u_s', u_a)}(f_x)} \right)^2} \right] \right\}$$

for the eight-frequency LUT, and

$$\min\left[\sqrt{\left(\frac{M_{measured}(f_x) - M_{(LUT:u_s', u_a)}(f_x)}{M_{(LUT:u_s', u_a)}(f_x)} \right)^2} + \sqrt{\left(\frac{R_{measured}(f_x) - R_{(LUT:u_s', u_a)}(f_x)}{R_{(LUT:u_s', u_a)}(f_x)} \right)^2} \right]$$

for the two-frequency LUT.

Fig. 3 Absorption variation experiment. True (solid line) versus extracted values for the two-frequency modulation/reflectance LUT (circles), eight-frequency modulation/reflectance LUT (triangles), and SDA (squares).
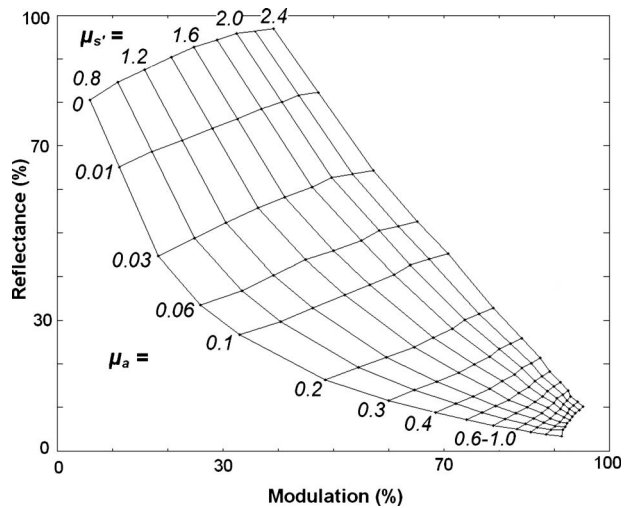
Fig. 2 Modulation/reflectance LUT generated using a spatial illumination period of 10 mm. The line intersections are measured data points. The lines are generated by linearly interpolating between data points.

3 Results and Discussion

3.1 Theoretical Motivation for the LUT

An accurate description of light propagation outside of the diffusion regime requires application of the radiative transport equation (RTE).[18] However, to our knowledge, a closed-form solution of the RTE does not currently exist for the geometry in question and current approximations are insufficient due to their inability to predict the diffuse reflectance close to the source. Although the P_3 approximation provides a good estimate at distances as close as 0.5 mm to the source,[19] it is insufficient for current wide-field applications, because the observed diffuse reflectance is a convolution of the reflectance from all source points over the entire imaging plane, and many diffusely reflected photons are remitted a very short distance away from the source. Application of the LUT serves as a pragmatic method for overcoming the mathematical hurdle of solving the RTE, facilitating the measurement of optical properties within and beyond the diffusion regime.

3.2 LUT Functionality

The plot in Fig. 2, which maps the measured modulation and reflectance values (M,R) into optical property values (μ_s',μ_a), is the empirical foundation for the modulation/reflectance LUT. It was generated using a spatial period of 10 mm. Importantly, it demonstrates that for a particular scatterer, each pair (M,R) maps uniquely to only one pair (μ_s',μ_a). It is worthwhile to note that (M,R) maps uniquely into (μ_s',μ_a) only because M is monotonically increasing in both μ_s' and μ_a, whereas R decreases monotonically in μ_a and increases monotonically in μ_s'.

The reason behind the observed monotonicity of M in μ_s' and μ_a is highly intuitive. Modulation is essentially a measure of how well the reflected sinusoidal photon density wave retains its original form (input amplitude). In turbid media, modulation increases with absorption due to enhanced photon confinement. Diffuse photons are less likely to be detected far away from their source due to absorption, which inhibits de-
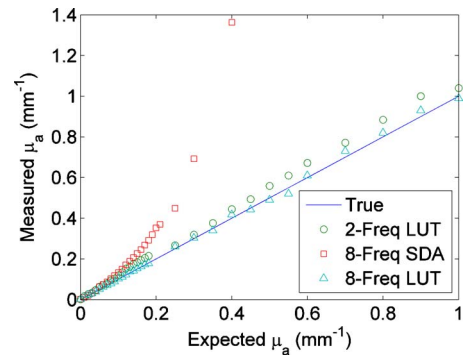
modulation of the reflected spatial sinusoid. Modulation increases with scattering due to enhanced photon escape. Both 0.35-μm spheres and tissue have high anisotropy values, and are thus highly forward scattering. Therefore, on average, multiple scattering events are required in order for incident photons to turn around and escape as diffusely reflected photons. Increased scattering ensures that these redirectional scattering events happen closer to the surface, enabling photons to reemerge closer to their source, thereby retaining modulation of the reflected spatial sinusoid. Higher absorption and scattering values result in increased modulation.

3.3 LUT Accuracy

The accuracy of the LUT was evaluated using the three validation sets described in Table 1. The first set of validation experiments characterizes the LUT's accuracy based on absorber type and μ_a (Fig. 3). The second set of validation experiments characterizes the LUT's accuracy based on μ_s' (Fig. 4). The third set of validation experiments characterizes the LUT's accuracy based on scatterer type (Fig. 5).

The accuracy of the LUT in extracting optical property values is compared directly to the accuracy of SDA in Figs. 3 (absorption variation) and 4 (scattering variation) for both the two-frequency LUT using the most accurate spatial period (10 mm) and the eight-frequency LUT. The data indicate that
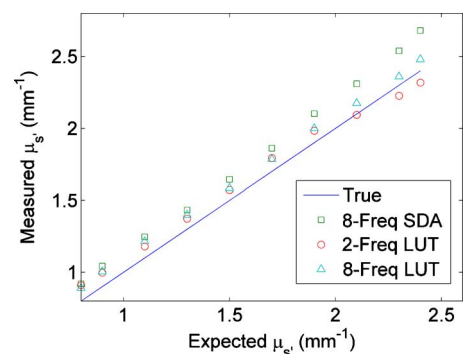

Fig. 4 Scattering variation experiment. True (solid line) versus extracted values for the two-frequency modulation/reflectance LUT (circles), eight-frequency modulation/reflectance LUT (triangles), and SDA (squares).
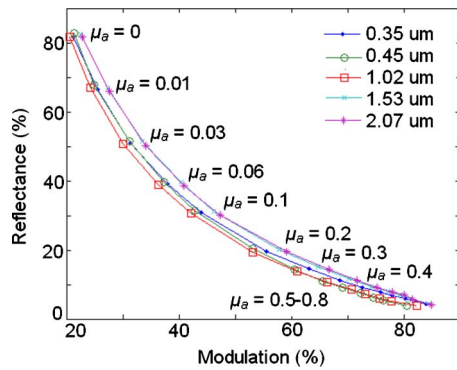
Fig. 5 Effect of microsphere size on measured modulation M and reflectance R at a spatial period of 10 mm for samples with identical (μ_s', μ_a).

Fig. 6 Effect of microsphere size on measured modulation M and reflectance R at a spatial period of 2 mm for samples with identical (μ_s', μ_a).

the eight-frequency LUT does not significantly increase measurement accuracy over the two-frequency LUT.

As shown in Fig. 3, both SDA and the LUT accurately extract absorption values at high albedos, where scattering exceeds absorption by a factor of 5 or more. In fact, for $(\mu_s'/\mu_a) > 10$, SDA is substantially more accurate than the LUT (rms error=2 versus 9%). Such errors in the LUT are likely caused by interpolation errors due to undersampling at high albedos, where reflectance falls off nonlinearly with increasing μ_a. At lower albedos, where $\mu_a \geqslant 0.3$ mm^{-1}, the LUT performs much better than SDA. With the high-albedo liquid calibration phantom employed (μ_s' = mm^{-1} and μ_a =0.033 mm^{-1}), SDA produces very large errors or can no longer extract a value for μ_a at $(\mu_s'/\mu_a) < 4$. Rms accuracy across the entire range is 7% for the two-frequency LUT and 6% for the eight-frequency LUT.

As shown in the scattering variation experiments detailed in Fig. 4, both the two-frequency LUT and eight-frequency LUT are more accurate than SDA, for measurements made with μ_a=0.5 mm^{-1}. Full range rms errors are 6, 6, and 12% for the two-frequency LUT, eight-frequency LUT, and SDA, respectively. The observation that system accuracy decreases at higher absorption values where the signal is lowest and the measurement uncertainty leads to larger errors is indicative of noise influencing the measurement. In practice, noise could be reduced by using a cooled CCD, averaging multiple frames, or binning over more pixels, but these alternatives would come at the expense of higher system costs, longer acquisition times, or decreased resolution.

Liquid phantoms were used to construct the LUT because they provide a well-controlled experimental model whereby μ_s', μ_a, and scatter phase function may all be varied independently.[20] However, it must be noted that we anticipate small inaccuracies in the recovered optical properties of samples that have different indices of refraction than the water-based phantoms employed (n=1.33). Given the slight refractive index mismatch between such phantoms and human tissue ($n \sim 1.4$),[21] we predict the errors incurred to be relatively small in light of the normally incident geometry of the system's projection and collection optics. It is instructive to note that the difference in normally incident specular reflectance between tissue (2.8%) and water (2%) is <1%. The corresponding maximum 1.6% fractional change in reflec-
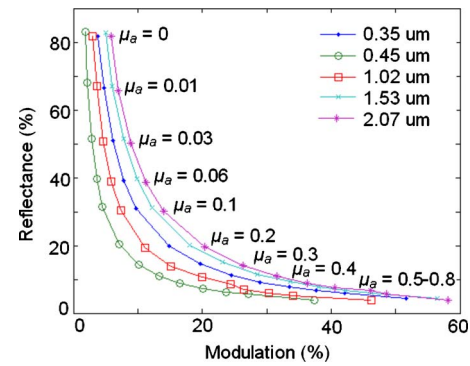
tance would produce errors of less than <2% in both absorption and scattering in a sample with μ_s'=1.5 mm^{-1} and μ_a =0.3 mm^{-1}.

3.4 Effect of Particle Size and Phase Function on Optical Property Extraction

The third set of validation experiments was used to characterize the effect of bead size (phase function) on the extracted optical property values. Bead diameters of 0.456, 1.02, 1.53, and 2.07 μm were selected to cover a range of scatterers characteristic of tissue (~ 0.4–2.0μm), as indicated by Mourant et al.[20] In this set of experiments, μ_s' was held constant at 1.0 mm^{-1} for all phantoms and μ_a was varied from 0–0.8 mm^{-1}. For measurements made on samples with identical optical properties (μ_s', μ_a), M and R should be identical. However, as shown in Fig. 5, the measured modulation and reflectance values at spatial periods of 10 mm are dependent on particle size and, hence, phase function, because the curves do not overlap. This effect becomes even more pronounced at shorter spatial periods (Fig. 6).

As shown in Figs. 5 and 6, the 0.356-μm spheres have modulation values intermediate to those of all other sphere sizes. On the basis of this observation, the LUT was constructed using 0.356-μm spheres in the interest of maximizing accuracy across a variety of particle sizes. If 0.456-μm spheres had been used, large errors would have resulted on
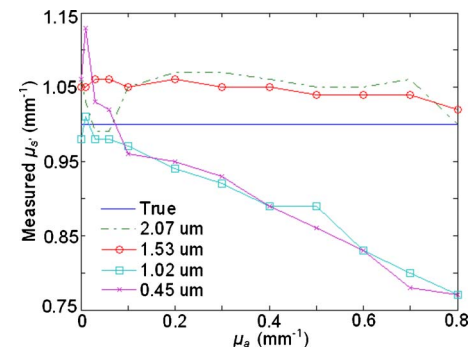

Fig. 7 Phase function variation experiment. True (solid line) versus extracted μ_s' values for 2.07 (dotted line), 1.53 (circles), 1.02 (squares), and 0.45 μm (exes) spheres versus μ_a.
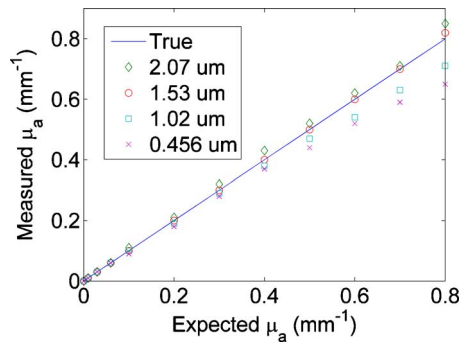
Fig. 8 Phase function variation experiment. True (solid line) versus extracted μ_a values for 2.07 (dotted line), 1.53 (circles), 1.02 (squares) and 0.45 μm (exes) spheres.

Fig. 9 Effect of LUT spatial period on extracting μ_a (circles) and μ_s' (squares).

validations with the 2.07-μm spheres. It is interesting to note that there appears to be no simple relationship between either g or the backscattering efficiency of each sphere and the observed modulation and reflectance. In light of this observation, we repeated the experiment with new spheres and found the results to be nearly identical.

The differences in M and R for identical (μ_s', μ_a) are not surprising given the results reported by others. In simulations of small source-detector optical probe measurements, Mourant et al. reported up to 60% differences in number of reflected photons for samples with $\mu_s' = 1.22$ and $\mu_a = 0$ mm^{-1}, depending on the phase function employed.[22] In simulations of spatially resolved reflectance measurements, Kienle et al. showed that errors in the derived (μ_s', μ_a) can be as large as 100% if the appropriate phase function is not taken into account.[23] In light of these observations, we analyzed the effect of the phase function on extracting (μ_s', μ_a) with the LUT. As shown in Figs. 7 and 8, the differences in the phase function of the scatterers can produce large errors in the recovered optical properties, particularly at low albedos, where errors of up to 23% in μ_s' and 12% in μ_a are observed. More accurate optical property measurement in this regime could be achieved with *a priori* knowledge of scatter phase function or with techniques capable of independently measuring scatterer phase function, such as multispectral Mie theory fitting of singly backscattered photons.[20,23,24]
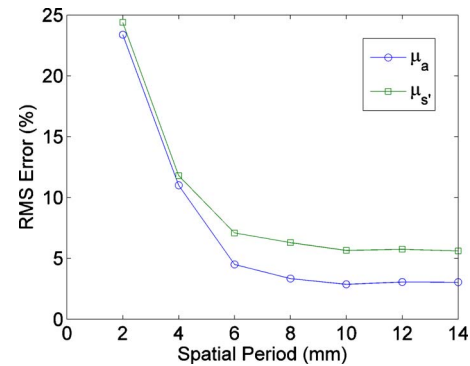
3.5 Optimization of LUT Spatial Period

The choice of illumination period has a significant effect on the LUT's accuracy, as alluded to in Fig. 6, where dramatically different modulation values are observed for the same (μ_s', μ_a). In order to analyze the effect of spatial period, the percent rms error for μ_s' and μ_a was calculated at each spatial period, for all bead sizes and optical property values shown in Figs. 7 and 8. The results, plotted in Fig. 9, indicate that a spatial period of 10 mm is optimal, where rms errors of 5.7 and 2.9% are observed for μ_s' and μ_a, respectively. However, as can be seen in Figs. 7 and 8, errors at lower albedos tend to be significantly higher than these rms error values reported over the full range ($\mu_a = 0$ to $\mu_a = 0.8$ mm^{-1}).

While large errors in the optical coefficients ($>20\%$) are recovered for the shortest illumination period (2 mm), it is worthwhile to note that measurements at such spatial periods may provide useful information about the phase function of the scatterers. Longer illumination periods sample longer photon pathlengths and are thus geared toward the detection of photons that have undergone multiple scattering events. Conversely, shorter illumination periods preferentially detect photons that have undergone fewer scattering events. As a result, such photons are likely to be singly backscattered[22] and thus contain valuable information about the phase function of the underlying scatterers. The phase function of the scatterers could potentially be used to determine the size of the scatter-
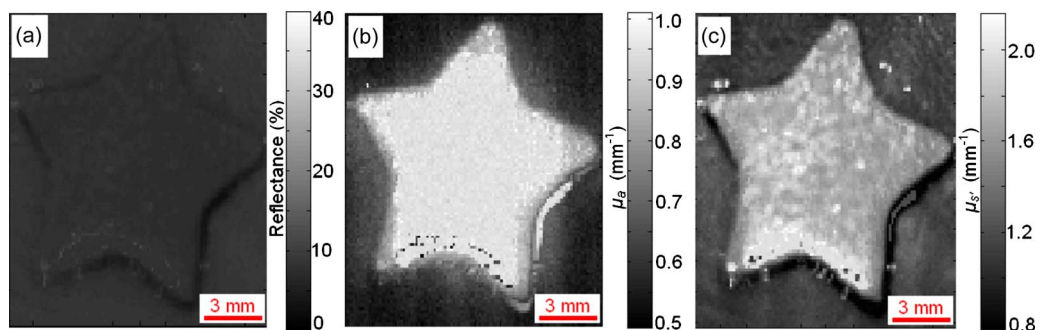

Fig. 10 (a) Raw dc reflectance image, the reflectance values of the star and surrounding medium are nearly identical and would thus appear indistinguishable to the naked eye. (b) Absorption map, the absorption coefficient in the star and surrounding medium are significantly different, and. (c) Scattering map, The scattering coefficient inside the star and surrounding medium are significantly different.

ers and hence be used to probe the microstructure of the underlying tissue for organelles of similar sizes.[20,24,25] The clinical potential of using short illumination periods (high spatial frequencies) will be subject to future studies.

3.6 LUT Imaging

Lastly, to illustrate the ability of the present technique to differentiate between low-albedo objects that appear nearly visually identical, a solid tissue phantom was analyzed. The phantom was prepared using 1.0-μm polystyrene spheres, Red 40, and agarose. As shown in the raw reflectance image [Fig 10(a)], the phantom consists of a star embedded in a surrounding medium. Both the star (μ_a=0.95 mm^{-1} and μ_s'=1.6 mm^{-1}) and the surrounding medium (μ_a=0.6 mm^{-1} and μ_s'=1.1 mm^{-1}) have reflectance values of roughly 10% and are thus very difficult to distinguish, except at the edges where a height mismatch causes shadowing effects. In order to realize accurate optical property extraction, it was necessary to bin the image pixels 5×5, in order to provide a sufficient signal to noise ratio. This was necessary due to the relatively low sample reflectance and our decision to utilize a low-cost, noncooled CCD.

Although the star and surrounding medium are difficult to distinguish in the reflectance image, the absorption [Fig 10(b)] and scattering [Fig. 10(c)] maps vividly illustrate the dramatic difference in the underlying optical properties. Quantitative optical property measurements can be used to noninvasively access valuable diagnostic information related to the disease state of tissue, including oxygen saturation, blood perfusion, melanin concentration, and tissue microarchitecture.[26–29]

The pixelation in these images is the result of low spatial sampling due to 5×5 pixel binning. In a clinical setting, hardware could be optimized for higher spatial sampling and shorter acquisition times by using a 16-bit cooled CCD, employing superluminescent LEDs, and increasing light throughput with antireflection-coated, high-NA lenses. It must be noted that the distinction between imaging resolution and optical property resolution is not trivial. Although imaging resolution is solely a function of collection optics and CCD resolution (given a sufficient signal to noise ratio), optical property resolution depends not only on CCD resolution, but also sample optical properties and the choice of spatial frequency. Although a precise relationship between the choice of spatial frequency and optical property resolution is yet to be determined, Bassi et al. have demonstrated that higher spatial frequencies (shorter spatial periods) correspond to enhanced localization of inhomogeneities in diffusive media.[30]

4 Conclusion

We have demonstrated an empirical, LUT-based approach to determining turbid sample optical properties that can be carried out using a traditional SFDI system. This technique, which is based solely on measured modulation and reflectance values for a set of samples that span the optical property range of interest, can be used to accurately and rapidly determine values of absorption and reduced scattering coefficient that may be encountered in tissue over a broad range of wavelengths. The LUT enhances the clinical diagnostic potential of SFDI by enabling quantitative determination of optical prop-

erties characteristic of human tissue at visible wavelengths with a single Spectralon calibration standard. Results presented here indicate that particle size (phase function) can affect the accuracy of extracted optical properties, especially at short spatial periods. As such, additional investigation of these effects is warranted.

References

1. D. Cuccia, F. Bevilacqua, A. Durkin, F. Ayers, and B. Tromberg, "Quantitation and mapping of tissue optical properties using modulated imaging," *J. Biomed. Opt.* **14**(2), 024012 (Mar./Apr. 2009).
2. D. Cuccia, F. Bevilacqua, A. Durkin, and B. Tromberg, "Modulated imaging: quantitative analysis and tomography of turbid media in the spatial-frequency domain," *Opt. Lett.* **30**, 1354–1356 (2005).
3. D. Toublanc, "Henyey-Greenstein and Mie phase functions in Monte Carlo radiative transfer computations," *Appl. Opt.* **35**, 3270–3274 (1996).
4. F. Ayers, D. Cuccia, K. Kelly, and A. Durkin, "Wide-field spatial mapping of *in vivo* tattoo skin optical properties using modulated imaging," *Lasers Surg. Med.* **41**, 442–453 (2009).
5. J. Weber, D. Cuccia, A. Durkin, and B. Tromberg, "Noncontact imaging of absorption and scattering in layered tissue using spatially modulated structured light," *J. Appl. Phys.* **105**, 102028 (2009).
6. S. Gioux, A. Mazhar, D. Cuccia, A. Durkin, B. Tromberg, and J. Frangioni, "Three-dimensional surface profile intensity correction for spatially modulated imaging," *J. Biomed. Opt.* **14**(3), 034045 (2009).
7. M. R. Treat, S. E. Amory, P. E. Downey, and D. A. Taliaferro, "Initial clinical experience with a partly autonomous robotic surgical instrument server," *Surg. Endosc* **20** (8), 1310–1314 (2006).
8. J. W. Tunnell and M. S. Feld, "Instrumentation for multi-modal spectroscopic diagnosis of epithelial dysplasia," *Technol. Cancer Res. Treat.* **2**(6), 505–514 (2003).
9. S. Flock, M. Patterson, B. Wilson, and D. Wyman, "Monte Carlo modeling of light propagation in highly scattering tissues—I: model predictions and comparison with diffusion theory," *IEEE Trans. Biomed. Eng.* **36**(12), 1162–1168 (1989).
10. W. Cheong, S. Prahl, and A. Welch, "A review of the optical properties of human tissue," *IEEE J. Quantum Electron.* **26**(12), 2166–2185 (1990).
11. R. M. P. Doornbos, R. Lang, M. C. Aalders, F. W. Cross, and H. J. C. M. Sterenborg, "The determination of *in vivo* human tissue optical properties and absolute chromophore concentrations using spatially resolved steady-state diffuse reflectance spectroscopy," *Phys. Med. Biol.* **44**, 967–981 (1999).
12. N. Rajaram, T. Nguyen, and J. Tunnell, "Lookup table-based inverse model for determining optical properties of turbid media," *J. Biomed. Opt.* **13**(5), 050501 (2008).
13. R. Reif, O. A'Amar, and I. Bigio, "Analytical model of light reflectance for extraction of the optical properties in small volumes of turbid media," *Appl. Opt.* **46**(29), 7317–7328 (2007).
14. R. Reif, M. Amorosino, K. Calabro, O. A'Amar, S. Singh, and I. Bigio, "Analysis of changes in reflectance measurements on biological tissues subjected to different probe pressures," *J. Biomed. Opt.* **13**, 010502 (2008).
15. P. S. L. Jacques, C. A. Alter, and S. A. Prahl, "Angular dependence of HeNe laser light scattering by dermis," *Lasers Life Sci.* **1**, 309–333 (1987).
16. R. Cubeddu, A. Pifferi, P. Taroni, A. Torricelli, and G. Vanentini, "A solid tissue phantom for photon migration studies," *Phys. Med. Biol.* **42**, 1971–1979 (1997).
17. C. F. Bohren and D. R. Hoffman, *Absorption and Scattering of Light by Small Particles*, Wiley, Hoboken, NJ (1983).
18. M. Patterson, B. Wilson, and D. Wyman, "The propagation of optical radiation in tissue I. models of radiation transport and their application," *Lasers Med. Sci.* **6**(155), 155–168 (1991).
19. E. Hull and T. Foster, "Steady-state reflectance spectroscopy in the

P_3 approximation," *J. Opt. Soc. Am. A* **18**(3), 584–599 (2001).

20. J. Mourant, J. Freyer, A. Hielscher, A. Eick, D. Shen, and T. Johnson, "Mechanisms of light scattering from biological cells relevant to non-invasive optical-tissue diagnostics," *Appl. Opt.* **37**, 3586–3593 (1998).

21. G. J. Tearney, M. E. Brezinski, J. F. Southern, B. E. Bouma, M. R. Hee, and J. G. Fujimoto, "Determination of the refractive index of highly scattering human tissue by optical coherence tomography," *Opt. Lett.* **20**(21), 2258–2260 (1995).

22. J. Mourant, J. Boyer, A. Hielscher, and I. Bigio, "Influence of the scattering phase function on light transport measurements in turbid media performed with small source-detector separations," *Opt. Lett.* **27**(7), 546–548 (1996).

23. A. Kienle, F. K. Forster, and R. Hibst, "Influence of the phase function on determination of the optical properties of biological tissue by spatially resolved reflectance," *Opt. Lett.* **26**, 1571–1573 (2001).

24. C. Mulvey and I. Bigio, "Wavelength-dependent backscattering measurements for quantitative real-time monitoring of apoptosis in living cells," *J. Biomed. Opt.* **14**(6), 064013 (Nov. 2009).

25. C. Yu, C. Lau, J. W. Tunnell, M. Hunter, M. Kalashnikov, C. Fang-Yen, S. Fulghum, K. Badizadegan, R. Dasari, and M. S. Feld, "As-sessing epithelial cell nuclear morphology by using azimuthal light scattering spectroscopy," *Opt. Lett.* **31**, 3119–3121 (2006).

26. N. Rajaram, T. Aramil, K. Lee, J. S. Reichenberg, T. H. Nguyen, and J. W. Tunnell, "Design and validation of a clinical instrument for spectral diagnosis of cutaneous malignancy," *Appl. Opt.* **142**(2), 142–152 (2009).

27. G. Zonios, J. Bykowski, and N. Kollias, "2001 Skin melanin, hemo-globin, and light scattering properties can be quantitatively assessed *in vivo* using diffuse reflectance spectroscopy," *J. Invest. Dermatol.* **117**, 1452–1457 (2001).

28. G. Zonios and A. Dimou, "Melanin optical properties provide evi-dence for chemical and structural disorder *in vivo*," *Opt. Express* **16**, 8263–8268 (2008).

29. L. T. Perelman and M. S. Feld, "Observation of periodic fine struc-ture in reflectance from biological tissue: a new technique for mea-suring nuclear size distribution," *Phys. Rev. Lett.* **80**(3), 627–630 (1998).

30. A. Bassi, C. D'Andrea, G. Valentini, R. Cubeddu, and S. Arridge, "Detection of inhomogeneities in diffusive media using spatially modulated light," *Opt. Lett.* **34**, 2156–2158 (2009).